Radiometric Calibration by Transform Invariant Low-rank Structure

Joon-Young Lee[1*] Boxin Shi[2] Yasuyuki Matsushita[3] In-So Kweon[1] Katsushi Ikeuchi[2]
[1] Robotics and Computer Vision Lab, KAIST, Korea
[2] The University of Tokyo, Japan
[3] Microsoft Research Asia, China
jylee@rcv.kaist.ac.kr, shi@cvl.iis.u-tokyo.ac.jp, yasumat@microsoft.com,
iskweon@ee.kaist.ac.kr, ki@cvl.iis.u-tokyo.ac.jp

Abstract

We present a robust radiometric calibration method that capitalizes on the transform invariant low-rank structure of sensor irradiances recorded from a static scene with different exposure times. We formulate the radiometric calibration problem as a rank minimization problem. Unlike previous approaches, our method naturally avoids over-fitting problem; therefore, it is robust against biased distribution of the input data, which is common in practice. When the exposure times are completely unknown, the proposed method can robustly estimate the response function up to an exponential ambiguity. The method is evaluated using both simulation and real-world datasets and shows a superior performance than previous approaches.

1. Introduction

In most cameras, there exists a radiometric response function that relates sensor irradiance and output brightness values. The function is typically designed to be non-linear for purposes such as compressing the dynamic range of sensor irradiance or for adapting to the display's non-linear mapping. While many computer vision algorithms assume linear (or affine) relationship between the sensor irradiance and the recorded intensity, the radiometric response functions are generally non-linear and unknown. Moreover, the shape of the functions may even vary with camera parameter settings. Therefore, radiometric calibration is an important first step for various computer vision algorithms that assume the linear relationship between the irradiance and observation to make them work correctly.

When multiple images are recorded from a static scene with different exposure times, the sensor irradiances at corresponding pixel locations are linearly related by the ratio of exposure times. If the response function is linear, the recorded pixel values (observations) show the linear relationship across the images. However, when the response function is non-linear, the linear relationship breaks down.

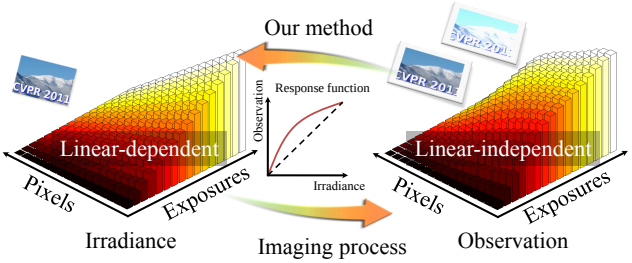

Figure 1. Illustration of our approach. Our method takes a set of images taken from a fixed view point with varying exposure times. In the matrix form, by putting images as column vectors, the irradiance matrix should be rank 1, while the observations matrix has the higher rank. Our method seeks the inverse response function that transforms the observation matrix into a low-rank matrix.

In this paper, we present a new radiometric calibration method that capitalizes on the fundamental linear dependency of sensor irradiances. Our method arranges the observations obtained from multiple exposure times in a matrix form, where a column corresponds to an image vector, and a row corresponds to a pixel location. When the linear relationship is observed in such a matrix, the rank of the matrix becomes one. On the other hand, when the response function is non-linear, the matrix generally becomes full rank. From this observation, we formulate the estimation of radiometric response functions as a rank minimization problem.

Contributions We show that the radiometric calibration problem can be robustly and efficiently solved by a rank minimization approach. Unlike previous approaches, we explicitly use the linear dependency of the irradiance vectors. Our rank minimization approach naturally avoids the over-fitting problem that is common in previous approaches that rely on the ℓ^2-norm minimization. In addition, the pro-

*This work was done while Joon-Young Lee was an intern at Microsoft Research Asia.

posed method can recover the response function up to an exponential ambiguity even when no information is available about the exposure times. Such recovered functions are useful for applications such as high-dynamic range image production and image stitching. In addition, we show that the same formulation can be applied to previous radiometric calibration approaches that use the linearity of the irradiance. As an example, we show the radiometric calibration from photometric stereo input images where the lighting directions vary across the images [15].

In presenting our work, we begin by briefly describing the radiometric response function and reviewing related works.

1.1. Radiometric response function

The radiometric response function relates the sensor irradiance I and recorded intensity value M (observation) by

$$M = f(I). \tag{1}$$

With assumptions of monotonicity and continuity, the response function f can be uniquely inverted to an inverse response function $g = f^{-1}$. With the inverse response function g, the recorded intensity values can be linearized by $g(M)$. Since what is available as input are the observations M, the radiometric calibration aims at recovering the inverse response function g.

1.2. Prior work

There are various approaches for radiometric calibration. One widely-used approach takes as input a set of images recorded with varying exposures from a fixed camera. The early work of Mann and Picard [10] used a gamma correcting function to represent response functions. With known exposure ratios, their method can successfully recover the inverse response function in the parametric form. Mitsunaga and Nayar used a different parametric representation, *i.e.*, a polynomial representation. Using an approximate knowledge of relative exposure times, their approach estimates response functions. Grossberg and Nayar [4] created a database of response functions (DoRF) and used it for better representation of response functions. Debevec and Malik [1] assumed a smoothness property of the response functions and estimated them in a non-parametric manner. There are a few prior approaches that allow some camera movement or scene motion. In Mann's [9] method, images are taken by a rotating and zooming camera. Kim and Pollefeys's method [5] allows for free movement of the camera and some motion in the scene.

As pointed out in [3, 5, 8], without the knowledge of exposure ratios, the estimate still has an *exponential ambiguity*. While not unique, such an estimate is still useful for many applications, such as radiometric alignment, HDR image production, and image stitching.

Instead of using varying exposure times, some approaches use statistical properties embedded in images to achieve radiometric calibration. Tsin *et al.*'s method [17] estimates non-parametric response functions using a statistical model of the CCD imaging process. Pal *et al.* [14] used probabilistic imaging models and weak prior models for deriving response functions to produce high-quality high dynamic range images. Matsushita and Lin [11] proposed to use the symmetric property of image noise by observing noise distributions contained in images. Takamatsu *et al.* [16] improved the noise-based method with a probabilistic intensity similarity measure, which requires fewer number of images. Lin *et al.* [6] and Lin and Zhang [7] proposed methods that take only a single image as input. Their methods use edges for obtaining color or gray-scale histogram distributions, and the optimal inverse response function is determined by transforming obtained non-linear distributions into linear distributions. A similar idea is recently introduced by Shi *et al.* [15] that achieves calibration from images taken under varying lighting conditions.

2. Low-rank Structure of Calibrated Observations

Our method casts the radiometric calibration problem as a low-rank structure recovery problem. Suppose we are given multiple images taken from a static scene with various exposures. The sensor irradiance I and observed intensity value M are related by a radiometric response function f by Eq. (1). Because the images are taken from a static scene, the scene radiance L is constant, and the sensor irradiance becomes proportional to the exposure time e with a constant scaling k:

$$I = kLe \propto e. \tag{2}$$

Consider an observation matrix $D \in \mathbb{R}^{m \times n}$, where m and n are the numbers of pixels and images, respectively, created by stacking all the vectorized images $\mathrm{vec}(M_i)$ as

$$D = \left[\mathrm{vec}(M_1) \mid \cdots \mid \mathrm{vec}(M_n)\right], \tag{3}$$

where $\mathrm{vec}(M_i) = [M_i(1), \cdots, M_i(m)]^T$ for $i = (1, \ldots, n)$. If we know an inverse radiometric response function $g = f^{-1}$, the observation matrix D can be transformed into an irradiance matrix A with a scaling ambiguity by

$$g \circ D = A = \left[\mathrm{vec}(I_1) \mid \cdots \mid \mathrm{vec}(I_n)\right], \tag{4}$$

where $\circ$ is an operator that describes the element-wise mapping. Since the irradiance vectors $\mathrm{vec}(I_i)$ should be linear-dependent, the rank of the irradiance matrix A becomes one. Therefore, our method seeks out the inverse response function g that minimizes the rank of the transformed matrix $g \circ D (= A)$ as

$$\hat{g} = \underset{g}{\mathrm{argmin}}\, \mathrm{rank}\,(A) \quad \text{s.t.} \quad A = g \circ D. \tag{5}$$

3. Calibration Algorithm

To efficiently compute the rank minimization problem of Eq. (5), previous approaches use an approximate solution method using a nuclear norm (sum of the singular values; $||A||_* \doteq \sum_{i=1}^{n} \sigma_i(A)$) minimization [18].

In our case, however, the nuclear norm minimization cannot be directly employed because the function g alters the absolute values of matrix elements, and it therefore results in the variations of the singular value magnitudes. To resolve this issue, we instead use condition numbers, *i.e.*, a ratio of singular values. We define the condition numbers as $\kappa_i(A) \doteq \sigma_i(A)/\sigma_1(A), \quad i = 2, 3, \ldots, n$. With the condition numbers, we can work with the relative magnitudes of the singular values that are unaffected by their absolute magnitudes. Now we approximate the energy functional (5) as a minimization of the summation of condition numbers as:

$$\hat{g} = \underset{g}{\operatorname{argmin}} \sum_{i=2}^{n} \kappa_i(A) \quad \text{s.t.} \quad A = g \circ D. \tag{6}$$

There are two main factors causing rank variations: non-linearity of response function and image noise. The top half of Table. 1 shows condition numbers from synthetic data that have five different exposure times. We assume the zero-mean Gaussian characteristics for image noise. Response functions in Fig. 2 are used as reference and we averaged the results of 100 trials for noisy cases. Fig. 2 (a) is an ideal linear response function. With this linear response function, all condition numbers are almost zero which means rank-1 structure. With other more general non-linear response functions, however, the condition number κ_2 becomes comparably larger than other condition numbers. This is commonly observed because of the monotonic and smooth characteristics of response functions. On the other hand, the effect of noise also changes the condition numbers. As shown in the bottom half of Table. 1, image noise makes all the condition numbers pretty even because of its high-frequency nature. From the above observations, our method only uses the condition number κ_2 instead of using all the condition numbers. Now the objective function is changed from Eq. (6) to

$$\hat{g} = \underset{g}{\operatorname{argmin}} \kappa_2(A) \quad \text{s.t.} \quad A = g \circ D. \tag{7}$$

To achieve a better convergence, we add more constraints to the objective functions as described in the next subsection.

3.1. Additional constraints

In general, response functions as well as inverse response functions are monotonic and smooth. To enforce the monotonicity of inverse response functions g, we put in a monotonicity constraint, which is represented as $\partial g/\partial M > 0$.

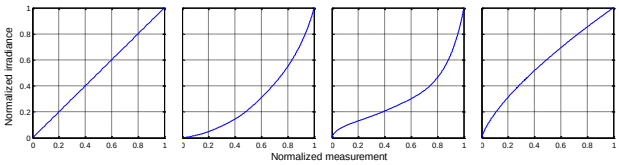

(a) (b) (c) (d)

Figure 2. Reference response functions used for Table. 1. (a) Ideal linear response function (RF 1). (b,c,d) General non-linear response functions (RF 2-4).

condition number		κ_2	κ_3	κ_4	κ_5
without noise	RF 1	0.0000	0.0000	0.0000	0.0000
	RF 2	0.0289	0.0034	0.0010	0.0005
	RF 3	0.1163	0.0177	0.0025	0.0001
	RF 4	0.0029	0.0000	0.0000	0.0000
with noise ($\sigma = 0.005$)	RF 1	0.0079	0.0077	0.0075	0.0072
	RF 2	0.0293	0.0059	0.0050	0.0048
	RF 3	0.1120	0.0175	0.0054	0.0046
	RF 4	0.0094	0.0087	0.0085	0.0081

Table 1. Condition number variations

In addition, we use the smoothness constraint for the inverse response function g as done in [1] to avoid the effect of noise. This smoothness constraint is represented as $\min \left|\partial g^2/\partial^2 M\right|$. The smoothness constraint, however, could cause under-fitting results in the case of complex response functions. Since the summation of the condition numbers is highly correlated to noise level as discussed above, we use the condition numbers for balancing the weight of the smoothness constraint. With these constraints, the final form of the objective function to estimate response function $\hat{g}$ is defined as

$$\hat{g} = \underset{g}{\operatorname{argmin}} \kappa_2(A) + \lambda_1 \sum_t H\left(-\frac{\partial g(t)}{\partial D}\right) + \lambda_2 \sum_{i=2}^{n} \kappa_i(A) \sum_t \left|\frac{\partial^2 g(t)}{\partial D^2}\right| \quad \text{s.t.} \quad A = g \circ D, \tag{8}$$

where $H(\cdot)$ is the Heaviside step function ($H(x) = 1$ when $x \geq 0$, and $H(x) = 0$, otherwise). The derivatives $\partial g(t)/\partial D$ and $\partial^2 g(t)/\partial D^2$ are assessed by sampling $g(t)$ at various t in the range of $[0, 1]$. The boundary conditions defined as $g(0) = 0$ and $g(1) = 1$ are embedded in parametric representation of g. More specifically, we represent the response function by a polynomial representation as done in [12] with the explicit boundary conditions:

$$g(t) = t + t(t-1) \sum_{i=1}^{n-1} c_i t^{n-i-1}, \tag{9}$$

where n is the order of a polynomial function, and c_i are the coefficients to estimate. To obtain a greater representation power, our method can alternatively use other representations, such as EMoR [4].

3.2. Exponential ambiguity

As discussed by Grossberg and Nayar in [2], recovery of the exposure ratios and the response function is impossible without making assumptions on the response function or having rough estimates on the exposure ratios. When exposure times are completely unknown, there remains an exponential ambiguity in the estimate. This exponential ambiguity means that if g is a solution of $I = g(M)$, then g^γ can also become a solution as $I^\gamma = g^\gamma(M)$ for any constant value γ. Our method also suffers from this exponential ambiguity like other methods when the exposure times are completely unknown, because the rank-1 structure is retained even after any exponential function is applied. In short, if $\mathrm{rank}(I) = 1$, then $\mathrm{rank}(I^\gamma) = 1$ for any γ.

However, without making any assumptions about exposure times, our method can robustly recover the response function up to the exponential ambiguity from at least two images. To resolve the ambiguity, our method only requires at least one exposure ratio. Using the known exposure ratio, we can estimate γ by solving the optimization problem described as

$$\hat{\gamma} = \underset{\gamma}{\mathrm{argmin}} \sum_{i,j} \left[\hat{g}^\gamma(M_i) - r_{i,j}\hat{g}^\gamma(M_j)\right]^2, \qquad (10)$$

where $r_{i,j}$ is the exposure ratio e_i/e_j of measurement pairs M_i and M_j.

4. Experiments

To evaluate the proposed method, we perform experiments using both simulation and real-world data. We compare our results with results of Mitsunaga and Nayar's method [12] (MN method, here-forth) as both methods take the same input. In our implementation, we used a 6^{th} order polynomial function to represent response functions as done in [12].

The optimization of Eq. (8) is performed using the Nelder-Mead simplex method [13]. We choose this method due to its simplicity, which can be implemented easily using a Matlab built-in function "fminsearch". In all the experiments, we use the linear function as the initial guess, and it is confirmed that the proposed method has a good convergence property even with such simple initialization. We always set $\lambda_1 = 1$ and $\lambda_2 = 1$ in Eq. (8) during the experiment. Once the response function is estimated up to the exponential ambiguity, we estimate the final response function using Eq. (10). This optimization is also performed using the Nelder-Mead simplex method [13].

4.1. Simulation

In this section, we use a synthetic dataset for quantitative evaluation. The synthetic dataset is generated using the DoRF database [4], which contains 201 measured response functions. We synthetically generate scene radiances in the range of $[0, 1]$ and create 1000 observations (which forms a 1000-pixel image) using each response function with five exposure times. The step of exposure ratios is set to 0.5 because this is a commonly available setting in commercial cameras. Fig. 3 shows scene radiance distribution of the synthetic dataset. To perform an evaluation, we add five different magnitudes of noise for each radiance distributions; therefore, a comparison with the MN method is performed using 1005 synthetic scenes in total. Gaussian noise with the standard deviation $\sigma(= 0, 0.0025, 0.0050, 0.0075, 0.01)$ is used for diversifying the datasets.

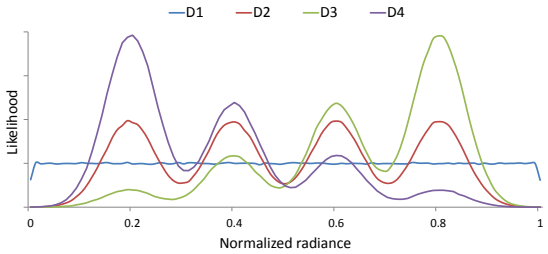

Figure 3. Scene radiance distributions of four synthetic datasets (D1-D4).

Results with synthetic dataset Fig. 4 shows results with the synthetic dataset. In this figure, we plot cumulative histograms that show the number of successful cases, *i.e.*, successful estimation of response functions under a certain root mean squared error (RMSE) with each configuration. As shown in the figure, the estimation performance is dependent not only on the noise level but also on the radiance distribution. With uniformly distributed scene radiance, the estimation becomes quite stable. However, when the radiance distribution is biased, which is very common, it introduces performance degradation as shown in the D4 result.

We summarize quantitative results in Table. 2. The DoRF database contains some response functions which are difficult to represent with 6^{th} order polynomials. These functions give trivial results for both our method and the MN method; therefore, we only use the best 150 fitting results for each of the algorithms to compute the mean and standard deviation of RMSE and disparity (the maximum deviation from the ground truth). The tables shows our method performs well for biased datasets (D2-D4), while the MN method works better with the uniform data (D1). Our method is robust against the increasing noise level, while the performance of the MN method rapidly degrades.

4.2. Real-world experiment

We also perform experiments using real-world cameras and scenes. In our experiments, we used four different cameras: Canon 20D, Nikon D70, Sony A200 and Olympus E-1. Each dataset is collected by capturing a static scene with different exposure times. Fig. 7 shows estimation results

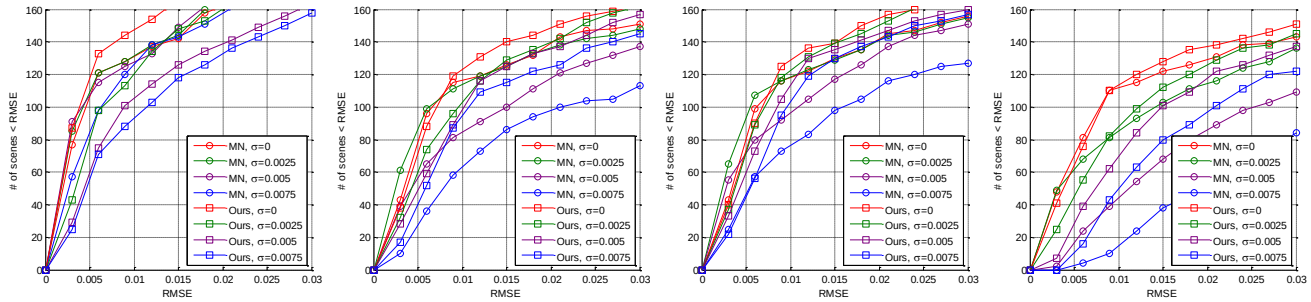

Figure 4. Cumulative histogram of the number of successful cases w.r.t. RMSE. From left to right, D1-D4 datasets are shown.

			Mean					Standard Deviation				
Sdv. of noise (σ)			0.0000	0.0025	0.0050	0.0075	0.010	0.0000	0.0025	0.0050	0.0075	0.0100
D1	RMSE	MN	0.0042	**0.0040**	**0.0044**	**0.0056**	**0.0083**	0.0042	0.0041	**0.0042**	**0.0039**	**0.0045**
		Ours	**0.0031**	0.0056	0.0081	0.0093	0.0119	**0.0023**	0.0041	0.0063	0.0070	0.0083
	Disparity	MN	0.0113	**0.0111**	**0.0118**	**0.0139**	**0.0188**	0.0113	0.0108	**0.0105**	**0.0110**	**0.0122**
		Ours	**0.0082**	0.0144	0.0196	0.0220	0.0270	**0.0065**	**0.0103**	0.0140	0.0161	0.0186
D2	RMSE	MN	0.0069	**0.0070**	0.0118	0.0177	0.0244	0.0067	0.0076	0.0104	0.0139	0.0177
		Ours	**0.0060**	0.0079	**0.0088**	**0.0105**	**0.0127**	**0.0048**	**0.0060**	**0.0064**	**0.0082**	**0.0098**
	Disparity	MN	0.0163	**0.0173**	0.0266	0.0402	0.0554	0.0161	0.0182	0.0230	0.0317	0.0396
		Ours	**0.0138**	0.0178	**0.0198**	**0.0240**	**0.0291**	**0.0111**	**0.0138**	**0.0145**	**0.0188**	**0.0229**
D3	RMSE	MN	0.0065	0.0062	0.0085	0.0134	0.0186	0.0062	0.0065	0.0076	0.0114	0.0132
		Ours	**0.0057**	0.0062	**0.0072**	**0.0084**	**0.0094**	**0.0043**	**0.0047**	**0.0050**	**0.0055**	**0.0061**
	Disparity	MN	0.0154	0.0152	0.0198	0.0303	0.0423	0.0150	0.0154	0.0168	0.0249	0.0302
		Ours	**0.0129**	**0.0141**	**0.0164**	**0.0191**	**0.0213**	**0.0100**	**0.0110**	**0.0122**	**0.0137**	**0.0147**
D4	RMSE	MN	0.0083	0.0115	0.0220	0.0350	0.0528	0.0088	0.0107	0.0166	0.0249	0.0358
		Ours	**0.0076**	**0.0107**	**0.0135**	**0.0178**	**0.0211**	**0.0071**	**0.0082**	**0.0096**	**0.0116**	**0.0126**
	Disparity	MN	0.0197	0.0263	0.0496	0.0767	0.1127	0.0214	0.0237	0.0362	0.0518	0.0709
		Ours	**0.0165**	**0.0219**	**0.0284**	**0.0374**	**0.0439**	**0.0150**	**0.0164**	**0.0203**	**0.0247**	**0.0284**

Table 2. Quantitative results using the synthetic dataset in comparison with Mitsunaga and Nayar's method (MN) in terms of the RMSE and disparity over various datasets.

# of samples		100	1000	10000
RMSE	MN	0.0261	0.0065	0.0022
	Ours	**0.0141**	**0.0042**	**0.0013**
Disparity	MN	0.0548	0.0139	0.0047
	Ours	**0.0295**	**0.0089**	**0.0029**

Table 3. Result of stability test using the blue channel of the scene Fig. 7 (a).

with real-world scenes. In the figure, the left column shows one of the input images, and the middle and right columns show the estimated response functions. For comparison, we also estimate the response function using MN method from the same data input. RMSE and disparity on the figures are calculated by comparing our result and the MN method's result by taking one of them as the ground truth. With reasonable data input, both methods present similar estimation results. For the evaluation of the stability with respect to the varying input data, we estimate the response function of Fig. 7 (a) using randomly sampled pixels (100, 1000, and 10000 pixels). For each sampled pixel number, we test 100 trials and calculate the RMSE and disparity of both methods. For this test, we use the median of the estimation results with 10000 samples as the ground truth because the experiment intends to test stability of the algorithms with different input data. The result using the blue channel is summarized in Table. 3. As shown in the table, our method produces stable estimates even when the number of sampled pixels is small.

Radiometric alignment One of the advantages of our calibration algorithm is that our method does not require any knowledge of exposure times when recovering the response function up to exponential ambiguity. Such estimates are useful for applications like radiometric alignment and image stitching. Here we show a radiometric alignment result using the estimated response function in Fig. 5. Without calibration, the aligned image with proper intensity normalization using the ratio of (R+G+B) intensity gives an RMSE of 0.2019. After calibration with our method, the error is reduced to 0.0385.

Figure 5. Radiometric alignment of real-world images. Top: input images, Bottom: radiometrically aligned images. For display, gamma correction($\gamma = 0.5$) is applied.

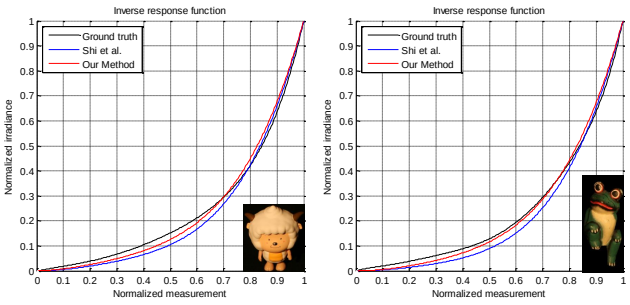

SHEEP (12) FROG (20)

Figure 6. Images of the real-world scene with the number of images used and radiometric calibration results by linearizing the color profiles.

5. Application to other radiometric calibration methods

The low-rank structure of the image irradiance matrix is a powerful cue for recovering response functions. Our method can be easily extended to deal with other radiometric calibration settings. In this section, we show an example of the extension by reformulating Shi *et al*. [15] for robustly deriving the solution using the rank minimization scheme.

Shi *et al*. [15] showed that the radiometric calibration for photometric stereo images can be performed by linearizing the color profiles. The color profile is defined as an ordered set of RGB color values in the RGB color space. Their method capitalizes on the property that color profiles form straight lines in the RGB color space if the response function is linear, while non-linear response functions f bend color profiles to non-linear shapes. Their method therefore seeks the inverse response function g that linearizes all the color profiles.

It is straightforward to cast their problem into our low-rank computation scheme. If the color profiles are stacked as row vectors to form a matrix, the linearization of color profiles becomes equivalent to the matrix rank minimization problem. More specifically, the color profile matrix should become rank-1 when the correct inverse response function is applied.

Following the notations of previous sections, we have an image stack matrix $D \in \mathbb{R}^{m \times n}$, and we still use m and n as the numbers of pixels and images. One difference is that the images are captured under n different lighting conditions. For each pixel, we have an n-dimensional row vector $\mathrm{vec}(D_i), \quad i = 1, \ldots, m$, and this time we extend each $\mathrm{vec}(D_i)$ into a $3 \times n$ vector to account for RGB color values. We denote this observation matrix as $D_i^{'}$. If a correct inverse response function g is given, it transforms the matrix $D_i^{'}$ to an irradiance matrix A_i, where $\mathrm{rank}(A_i) = 1$. Involving all the pixels, we have the objective function written as:

$$\hat{g} = \underset{g}{\mathrm{argmin}} \sum_{i=1}^{m} \mathrm{rank}\,(A_i) \quad \text{s.t.} \quad A_i = g \circ D_i^{'}. \quad (11)$$

Thus, the problem can be solved in exactly the same way as discussed in previous sections.

To verify the robustness and effectiveness of our method, we performed experiments on two real-world scenes, SHEEP and FROG, recorded by a Canon 20D and Nikon D70, respectively. The ground truth is obtained by the MN method using a Macbeth Color Chart and the experiment was performed on an Intel Core2 Duo E6750 (2.66GHz) CPU.

For each configuration, we randomly select samples to produce color profiles and compute the average of the results of ten trials. In practice, the accuracy of the Shi *et al*.'s method has dependency on the selected samples, therefore we take more trials and remove obvious failure modes. Fig. 6 shows the results. The median response curve of ten trials is used for plotting in the figure. We summarize the quantitative results in Table. 4. For both datasets, our method shows more accurate and stable results. With a small number of samples, the result of the original method fluctuates because of the heuristic nonlinearity constraint, but our method robustly converges well because of the computation scheme. With more samples, both methods give more stable and robust estimation. As shown in the table, our method is about 1000 times faster than the original method. Since our method has a computational complexity of $O(n)$, we can use more samples to achieve robust estimation.

6. Conclusions

In this paper, we have introduced a robust radiometric calibration algorithm that uses the low-rank structure of irradiance vectors. The problem is formulated as a rank minimization and solved by minimization of the condition number of the input matrix. Our method can robustly estimate response functions; when the exposure times are completely unknown, it can estimate the response functions up to an exponential ambiguity. The advantage of our method is that it can avoid over-fitting because our method does not rely on the traditional least-square fitting. Additionally, we show

Dataset		SHEEP (Canon 20D)			FROG (Nikon D70)		
Method	samples	RMSE (std.)	Disparity (std.)	Time(s)	RMSE (std.)	Disparity (std.)	Time(s)
Shi *et al.*	50	0.0488 (0.0227)	0.0846 (0.0429)	284.01	0.0279 (0.0050)	0.0456 (0.0064)	478.67
	100	0.0418 (0.0172)	0.0729 (0.0345)	595.42	0.0293 (0.0038)	0.0441 (0.0056)	891.97
Our method	50	0.0219 (0.0002)	0.0429 (0.0027)	0.27	0.0183 (0.0007)	0.0393 (0.0027)	0.36
	100	0.0218 (0.0002)	0.0423 (0.0022)	0.40	0.0176 (0.0004)	0.0390 (0.0023)	0.60

Table 4. Radiometric calibration results by linearizing the color profiles. SHEEP/FROG dataset captured by Canon 20D and Nikon D70 are used. Ten trial results are averaged. The value inside the brackets is the standard deviation of ten trials.

that our framework can be applied to other radiometric calibration problems that use linearization of observations by taking Shi *et al.*'s method as an example. The effectiveness of the proposed approach is verified using both simulation and real-world experiments.

Limitations Since our method is based on low-rank structure of irradiances, the result of our method always converge to the direction of minimal rank. As we mentioned before, rank variations can be observed due to both nonlinear response function and image noise. Therefore, the rank could be more affected by noise when the non-linearity of the response function is negligible compared with the noise level, and in such a case, our method could produce inaccurate estimation.

In current implementation, we use a simple optimizer for the rank minimization, and it is usually sufficient to find the right solution as shown in experiments. However, sometimes the optimization fails to converge to the global solution, or converges to a trivial solution due to insufficient input data or great noise. This could be improved by using a better optimization method for the rank minimization.

Acknowledgements

The first author is partially supported by MKE(The Ministry of Knowledge Economy), Korea, under the Human Resources Development Program for Convergence Robot Specialists support program supervised by the NIPA(National IT Industry Promotion Agency) (NIPA-2010-C7000-1001-0007). The authors would like to thank Zhengdong Zhang for helpful discussions.

References

[1] P. Debevec and J. Malik. Recovering high dynamic range radiance maps from photographs. In *Proc. of ACM SIGGRAPH*, pages 369–378, 1997. 2, 3

[2] M. Grossberg and S. Nayar. What can be known about the radiometric response from images? In *Proc. of European Conf. on Comp. Vis. (ECCV)*, pages 189–205, 2002. 4

[3] M. Grossberg and S. Nayar. Determining the camera response from images: What is knowable? *IEEE Trans. on Pattern Analysis and Machine Intelligence*, 25(11):1455–1467, 2003. 2

[4] M. Grossberg and S. Nayar. What is the space of camera response functions? In *Proc. of Comp. Vis. and Pattern Rec. (CVPR)*, pages 602–609, 2003. 2, 3, 4

[5] S. Kim and M. Pollefeys. Robust radiometric calibration and vignetting correction. *IEEE Trans. on Pattern Analysis and Machine Intelligence*, 30(4):562–576, 2008. 2

[6] S. Lin, J. Gu, S. Yamazaki, and H. Shum. Radiometric calibration from a single image. In *Proc. of Comp. Vis. and Pattern Rec. (CVPR)*, pages 938–945, 2004. 2

[7] S. Lin and L. Zhang. Determining the radiometric response function from a single grayscale image. In *Proc. of Comp. Vis. and Pattern Rec. (CVPR)*, pages 66–73, 2005. 2

[8] A. Litvinov and Y. Schechner. Addressing radiometric nonidealities: a unified framework. In *Proc. of Comp. Vis. and Pattern Rec. (CVPR)*, pages 52–59, 2005. 2

[9] S. Mann. Comparametric imaging: Estimating both the unknown response and the unknown set of exposures in a plurality of differently exposed images. In *Proc. of Comp. Vis. and Pattern Rec. (CVPR)*, pages 842–849, 2001. 2

[10] S. Mann and R. Picard. On being 'undigital' with digital cameras: extending dynamic range by combining differently exposed pictures. In *Proc. of IS & T, 48th annual conference*, pages 422–428, 1995. 2

[11] Y. Matsushita and S. Lin. Radiometric calibration from noise distributions. In *Proc. of Comp. Vis. and Pattern Rec. (CVPR)*, pages 1–8, 2007. 2

[12] T. Mitsunaga and S. Nayar. Radiometric self-calibration. In *Proc. of Comp. Vis. and Pattern Rec. (CVPR)*, pages 374–380, 1999. 3, 4

[13] J. Nelder and R. Mead. A simplex method for function minimization. *Computer Journal*, 7:308–313, 1965. 4

[14] C. Pal, R. Szeliski, M. Uyttendale, and N. Jojic. Probability models for high dynamic range imaging. In *Proc. of Comp. Vis. and Pattern Rec. (CVPR)*, pages 173–180, 2004. 2

[15] B. Shi, Y. Matsushita, Y. Wei, C. Xu, and P. Tan. Self-calibrating photometric stereo. In *Proc. of Comp. Vis. and Pattern Rec. (CVPR)*, pages 1118–1125, 2010. 2, 6

[16] J. Takamatsu, Y. Matsushita, and K. Ikeuchi. Estimating camera response functions using probabilistic intensity similarity. In *Proc. of Comp. Vis. and Pattern Rec. (CVPR)*, pages 1–8, 2008. 2

[17] Y. Tsin, V. Ramesh, and T. Kanade. Statistical calibration of ccd imaging process. In *Proc. of Int'l Conf. on Comp. Vis. (ICCV)*, pages 480–487, 2001. 2

[18] J. Wright, A. Ganesh, S. Rao, Y. Peng, and Y. Ma. Robust principal component analysis: Exact recovery of corrupted low-rank matrices by convex optimization. In *Proc. of Neural Information Processing Systems*, 2009. 3

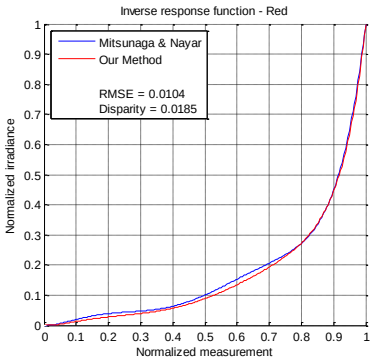

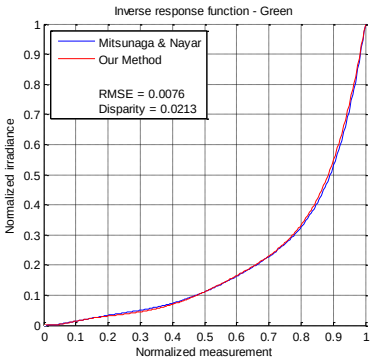

(a) Canon 20D

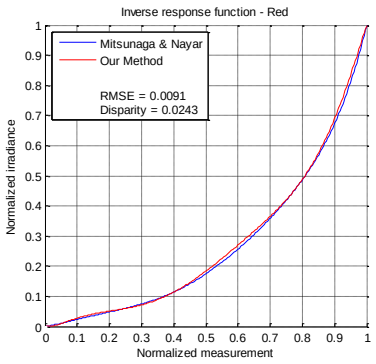

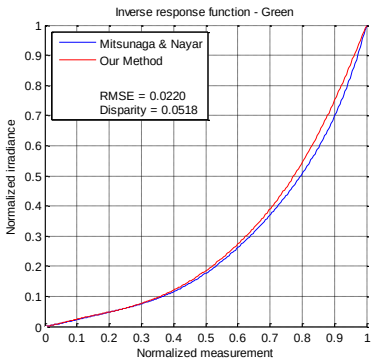

(b) Nikon D70

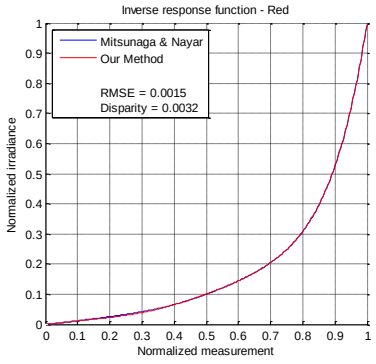

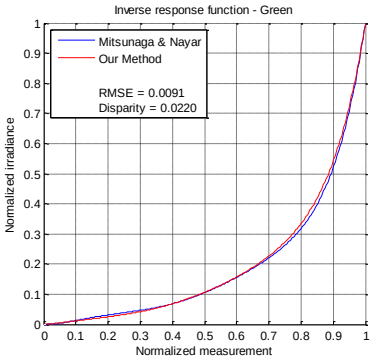

(c) Sony A200

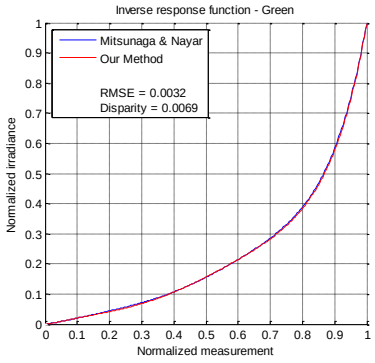

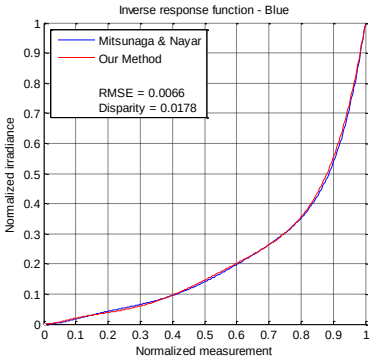

(d) Olympus E-1

Figure 7. Results of our calibration method. Left column: One of the input images. Middle/right column: Estimated inverse response functions. The RMSE and disparity are calculated by comparing our estimation and the MN method's estimation. From top to bottom, the results of different cameras are shown: (a) Canon 20D, (b) Nikon D70, (c) Sony A200, and (d) Olympus E-1.